In Situ Synthesis of Porous Fe$_3$O$_4$/C Microbelts and Their Enhanced Electrochemical Performance for Lithium-Ion Batteries

Leiming Lang[†,‡] and Zheng Xu*[,†]

[†]State Key Laboratory of Coordination Chemistry and Nanjing National Laboratory of Microstructure, School of Chemistry and Chemical Engineering, Nanjing University, Nanjing 210093, P. R. China

[‡]Biochemical and Environmental Engineering College, Nanjing Xiaozhuang University, Nanjing, 211171, P. R. China

S *Supporting Information*

ABSTRACT: The porous Fe$_3$O$_4$/C microbelts (FCBs) were synthesized by simple electrospinning method, combined with carbonization of the precursor microbelts at high temperature in N$_2$ flow. Compared with α-Fe$_2$O$_3$ microbelt, the FCBs show better cyclic performance. The high capacity of 710 mA h g^{-1} is still maintained after 50 cycles. The excellent performance of FCBs in lithium-ion batteries can be attributed to the highly stable porous belt structure of FCBs and to the substantial structure carbon matrix surrounded Fe$_3$O$_4$ nanoparticles. The synthesis method is simple, cheap, and green and could be extended to fabricate other carbon composites.

KEYWORDS: *electrospinning, iron oxide/carbon microbelt, electrochemistry, lithium-ion battery*
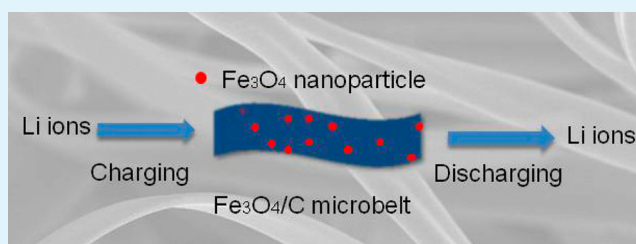
1. INTRODUCTION

The rechargeable Li-ion battery (LIB) has attracted intensive research interest because of its broad applications in energy storage devices for electric, hybrid electric vehicles, and intermittent renewable energy sources due to their high energy and power densities and long cycle lifetime.[1−5] The current generation of LIBs is based on electrode materials in which Li$^+$ is stored by insertion between structural layers during charging and extracted from the layers during discharging without significant structural change to show excellent cycling performance. In recent years, great efforts have been paid to design high performance electrode materials in terms of energy capacity and cycling stability, such as transition-metal oxides Co$_3$O$_4$,[6−9] SnO$_2$,[10−12] FeO$_x$,[13−19] MnO$_2$,[20−22] TiO$_2$,[23,24] and so on.[25−27] Among them, iron oxides micro/nano materials, such as hematite (α-Fe$_2$O$_3$) and magnetite (Fe$_3$O$_4$), have been extensively studied as potential electrode materials due to their higher theoretical capacities (1004 mA h g^{-1} for α-Fe$_2$O$_3$ and 924 mA h g^{-1} for Fe$_3$O$_4$), low toxicity and lower cost. Although they have high charge−discharge capacity, their cycle performance cannot keep stable and the capacities fast fade, resulting from the poor electronic conductivity and large volume variation during the conversion reaction process. To improve the durability and high rate capability of transition metal oxides, various types of nanostructures have been employed as anode materials for LIBs. In order to mitigate the large volume variation problem of transition metal oxides and to increase the electronic conductivity, carbon coatings have been extensively explored.[25,28−40] However, the compact carbon coatings on nanoparticles cannot allow residual buffer space to accommodate the large volume change of Fe$_3$O$_4$ nanoparticles during Li$^+$ insertion/extraction. Thus, it remains

necessary to exploit an approach for the fabrication of suitable carbon matrix to accommodate volume expansion upon Li$^+$ insertion as well as to increase the electronic conductivity.[41−43]

As we all know, electrospinning provides an inexpensive, simple, and versatile technique to obtain various fibers including polymer, metal oxide, and organic−inorganic composites.[1,44−49] Recently, we are devoted to develop a facile method for construction of metal oxide 1D nano/micro-structure by using noncoaxial electrospinning and the fibers with various morphologies including porous nanowires, nanotubes, and tube-in-tube have been prepared.[50] Now, we are interested to extend this method into the synthesis of 1D composite of metal oxide/C and exploit their electrochemical performance.

In this paper, we focus on the synthesis of Fe$_3$O$_4$/C microbelts by simple electrospinning technology and their electrochemical performance. The composites with microbeltlike structure fabricated by electrospinning technology have never been reported before. What's more, the porous structure can be formed by calcination of the precursor microbelts and Fe$_3$O$_4$ nanoparticles can be wrapped by carbon effectively by in situ reduction, which is of benefit to improve the charge−discharge capacity of LIBs. The prepared Fe$_3$O$_4$/C microbelts exhibit superior electrochemical properties as an electrode material in LIBs.

2. EXPERIMENTAL SECTION

2.1. Materials. Poly(vinyl pyrrolidone) (PVP-K30, Mn 58000), iron nitrate ($Fe(NO_3)_3$), acetic acid (HAc), ferric chloride ($FeCl_3$), ferrous chloride ($FeCl_2$), $NH_3 \cdot H_2O$ (30%), and ethanol (≥99.9%) were all purchased from Sigma-Aldrich Chemical Co. They were all analytic grades and not further purified for use.

2.2. Synthesis of Porous Fe_3O_4/C Microbelts (FCBs). To synthesize the $Fe(NO_3)_3$−PVP precursor microbelts, we prepared the ethanol solution containing PVP and metal nitrate for eletrospinning. In a typical procedure, 1.75 g PVP and 1.0 g $Fe(NO_3)_3$ were dissolved in 7 mL ethanol and 1 mL acetic acid completely with constant stirring and ultrasonication to obtain a transparent homogeneous solution. The prepared solution was delivered to a pipet equipped with a needle made of stainless steel which the pinhead is approximately 0.5 mm. Then, the pipet was driven using a peristaltic pump at a constant flow rate of 0.3 mL min⁻¹. The needle was connected to a high-voltage power and the aluminum foil was placed 20 cm from the tip of the needle vertically in order to collect the microbelts. Under a high-voltage electric field of 15 KV, a droplet with charge suspended from the tip of the pipet was ejected out in the form of microbelts and the final $Fe(NO_3)_3$−PVP microbelts were deposited on to the collector. Usually, fiberlike precursor can be obtained by eletrospinning, whereas the microbelts can only be fabricated under suitable eletrospinning solution viscosity. Finally, the porous FCBs can be achieved by the calcination of the prepared microbelt-precursor at 500 °C for 2 h in N_2 flow at the rate of 2 °C min⁻¹ from room temperature, while α-Fe_2O_3 microbelts are obtained when the precursor microbelts are calicined in air under the same conditions.

2.3. Preparation of Fe_3O_4 Nanoparticles. The Fe_3O_4 nanoparticles were synthesized by a simple coprecipitation method. In typical procedure, Fe^{3+} and Fe^{2+} chlorides were mixed at the molar ratio of 2:1 in deionized water. The excess $NH_3 \cdot H_2O$ (30%) was added to the mixed solution at 40 °C under N_2 atmosphere with constantly magnetic stirring. The resulting products were centrifuged and washed with distilled water repeatedly and finally dried at 80 °C in air for characterization.

2.4. Characterization. The morphologies of the products were characterized by scanning electron microscopy (SEM) (EDAX-4800) and transmission electron microscopy (TEM) (Japan JEOL JEM-200CX, transition electron microscope). The high-resolution TEM (HRTEM) images were obtained using a JEOL-2010 TEM at an acceleration voltage of 200 kV. The phase purity of the products were characterized by X-ray power diffraction (XRD), (Shimadzu XD-3A X-ray diffractometer with Cuα radiation, λ = 0.15417 nm), and the energy dispersive spectrum (EDS) was recorded on EDAX-4800. The BET (Brunauer−Emmett−Teller) surface area was measured by ASAP2020 (Micromeritics, United States). Thermogravimetric analysis was carried on LABSYS from SETERAM. The cross-sectional compositional line profiles (CSCLPs) were studied on TECNAI F20 S-TWIN field emission gun transmission electron microscopy (STEM), which is equipped with EDX apparatus.

2.5. Electrochemical Measurements. Galvanostatic measurements were carried out using two-electrode cells with lithium metal as the counter electrode. The working electrodes were fabricated by compressing the mixture of 85 wt % active materials, 10 wt % acetylene black, and 5 wt % ploytetrafluoroethylene (PTFE) onto an circular copper foil of 8 mm in diameter. The foils were dried in vacuum at 100 °C for at least 10 h and then assembled as cells in an Ar-filled Labconco glovebox. The electrolyte solution was 1 M $LiPF_6$ dissolved in a mixture of ethylene carbonate (EC), dimethyl carbonate (DMC), and ethylene methyl carbonate (EMC) with the volume ratio of EC:DMC:EMC = 1:1:1. The galvanostatic charge/discharge tests were performed with a Land CT2001 battery tester at different current densities in a voltage range of 3.5−0.01 V at 25 °C.

3. RESULTS AND DISCUSSION

An X-ray diffraction (XRD) analysis is used to determine the chemical composition and phase structure of the sample. Figure 1 is the X-ray diffraction (XRD) pattern of porous Fe_3O_4/C

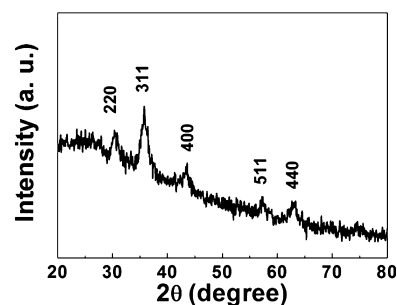**Figure 1.** X-ray diffraction (XRD) pattern of porous Fe_3O_4/C microbelt.

microbelts (FCBs) over the range $20° \leq 2\theta \leq 80°$ (2θ). The diffraction peaks at 30.1°, 35.5°, 43.1°, 57.0°, 62.6° (2θ) correspond to (220), (311), (400), (511), (440) crystal planes of Fe_3O_4, which is in good agreement with the standard XRD pattern of Fe_3O_4 (JCPDS: 82-1533). No observation of C diffraction peak is due to the formation of amorphous carbon during calcination. The high background of the XRD pattern attributes to the low crystallization of Fe_3O_4 nanoparticles, but no organic molecular contribution, because the organic molecular was carbonized completely at 500 °C.

The morphology and microstructure of the sample were observed by scanning electron microscopy (SEM) and transmission electron microscopy (TEM). Figure 2 shows the
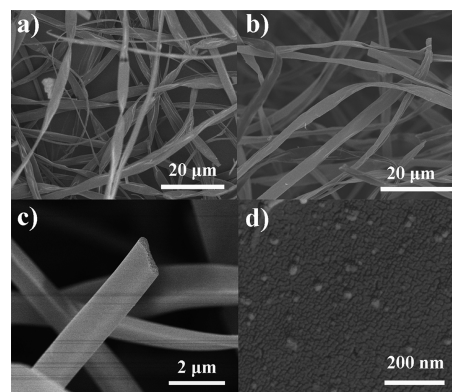

Figure 2. (a) SEM image of the precursor microbelts composed of PVP and $Fe(NO_3)_3$ by electrospinning. (b) Low-magnification SEM image of as-prepared porous Fe_3O_4/C microbelt after calcination at 500 °C for 2 h in N_2 flow. (c) Cross-section SEM image of an individual FCB. (d) Magnified SEM image of an individual microbelt from the sample in part b, showing the porous structure of Fe_3O_4/C mcirobelt clearly.

SEM images of the prepared different samples. Figure 2a is the image of $Fe(NO_3)_3$−PVP precursor microbelts with ~4 μm width synthesized by eletrospinning. Figure 2b is the SEM image of Fe_3O_4/C microbelts after calcination at 500 °C for 2 h in N_2 flow. Compared with precursor microbelts, no obvious width change of the Fe_3O_4/C microbelts indicates that the beltlike structure of the product still remains well after calcination (Figure 2c). Fe_3O_4 nanoparticles can be found on the surface of a Fe_3O_4/C microbelt in the magnified SEM image in Figure 2d and STEM (Supporting Information Figure S1a). The cross-sectional compositional line profiles of EDX line scan measured along the arrowhead marked in Figure S1a show the broad peaks of Fe and O elements with an obvious

valley corresponding to the gap between two Fe_3O_4 nanoparticles (Figure S1b). The structure of the porous FCBs was further investigated by TEM and high-resolution TEM (HRTEM). Figure 3a is TEM image of an individual porous
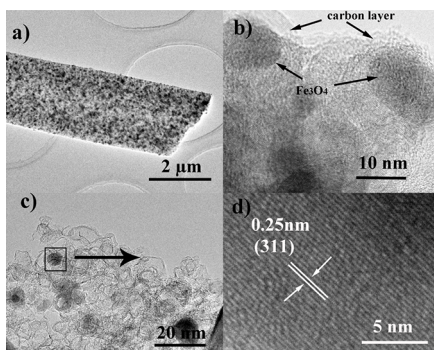

Figure 3. (a) TEM image of individual porous Fe_3O_4/C microbelt. (b and c) The magnified TEM images of FCB. (d) HRTEM image of the Fe_3O_4 nanoparticle as marked with the blackframe in part c.

FCB, from which we can see that the microbelt is composed of many nanoparticles. The magnified TEM images of the FCB show Fe_3O_4 nanoparticles are wapped by carbon layer effectively (Figure 3b) and porous structure can be seen obviously (Figure 3c). As seen from the HRTEM image (Figure 3d), the interplanar spacings of 0.25 nm agree well with the spacing of (311) lattice plane of Fe_3O_4. The Fe_3O_4 nanoparticles are surrounded by an amorphous carbon layer to prevent them from aggregation. For contrast, the α-Fe_2O_3 microbelts can be obtained by calcination of the precursor microbelts in air under the same conditions, and the SEM image shows the similar morphology and size to FCBs (Supporting Information Figure S2).

The energy dispersive spectra (EDS, Figure 4a, S3) reveal that the sample is composed of C, Fe, and O elements. The

relative intense signal of C belongs to the carbon matrix formed by carbonization of PVP at N_2 flow. Thermogravimetric (TG) analysis was carried out to display the conversion process from $Fe(NO_3)_3$–PVP microbelts to FCBs. Three obvious weight loss processes can be observed from the TG and DTA of as-synthesized precursor (Figure 4b). The first mass loss appears before 200 °C, which is ascribed to the degradation of the side chain of PVP and the evaporation of ethanol and a little water.[51] The following obvious weight loss between 200 and 250 °C is mainly attributed to the decomposition of $Fe(NO_3)_3$ (eq 1).[38,44] The further weight loss between 250 and 450 °C is due to the degradation and carbonization of the main chain of PVP and the generation of Fe_3O_4 ascribed from the reaction between C and Fe_2O_3 (eq 2). When the temperature is higher than 450 °C, no obvious weight loss was observed indicating that the precursor is converted to Fe_3O_4/C microbelts completely. Figure 4c is TG-DTA curves of FCBs, from which about 45% weight percentage of Fe_3O_4 in the composite can be calculated. The peaks at 1363 and 1585 cm^{-1} in Raman spectrum demonstrate the existence of carbon in FCBs (Figure 4d).

$$4Fe(NO_3)_3 \rightarrow 2Fe_2O_3 + 12NO_2 + 3O_2 \qquad (1)$$

$$C + 6Fe_2O_3 \rightarrow 4Fe_3O_4 + CO_2 \qquad (2)$$
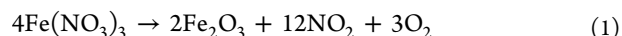
The N_2 adsorption/desorption isotherm in Figure 5 shows a type IV curve with a hysteresis loop. The BET (Brunauer–Emmett–Teller) surface area and single point total pore volume are 174.6 and 0.11 cm^3 g^{-1}, respectively. The high surface area and typical mesoporous structure indicate that somewhat improved electrochemical performances of anode material in LIBs should be expected.[52,53]

The electrochemical impedance spectra (EIS) studies of the FCBs and α-Fe_2O_3 microbelts were carried out on the cell comprising the samples as the working electrode versus Li before the discharge–charge cycle. The results are presented as Nyquist plots (Z' vs $-Z''$), where Z' and Z'' refer to the real
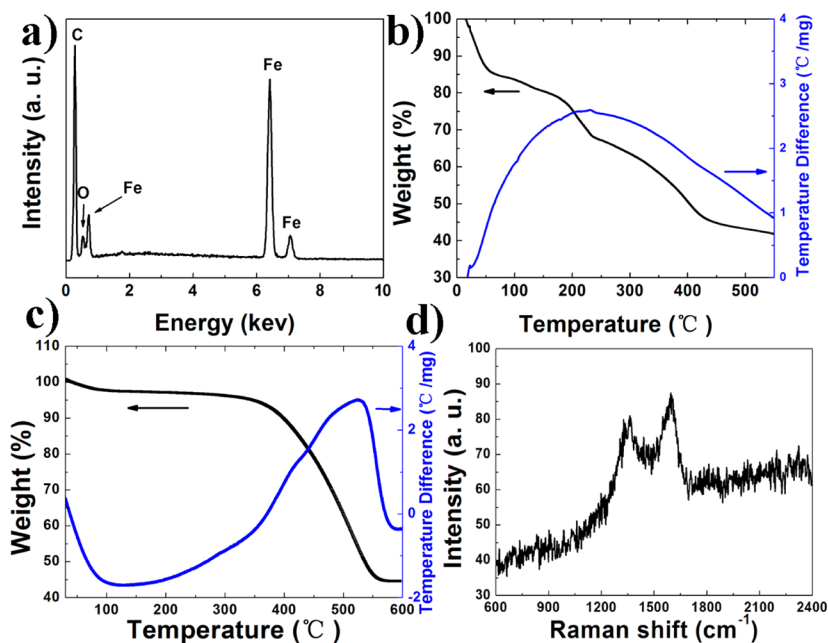

Figure 4. (a) EDS spectrum of FCBs. TG-DTA curves: (b) precursor microbelts composed of PVP and $Fe(NO_3)_3$ and (c) Fe_3O_4/C microbelt. (d) Raman spectrum of FCBs.
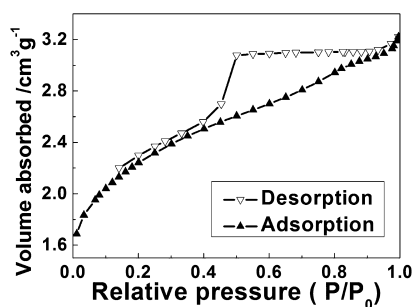
Figure 5. Nitrogen adsorption/desorption isotherm of Fe_3O_4/C microbelts.

and imaginary parts of cell impedance, respectively. The typical characteristics of the two Nyquist plots are one semicircle in the high frequency range and a sloping straight line in the low frequency range. An intercept at the Z' axis in high frequency corresponds to the resistance of the electrolytes. The radius of the semicircles of FCBs electrode is smaller than those of pure Fe_2O_3 and Fe_3O_4 nanoparticle electrode (Figure 6a), which indicates that the lower charge-transfer resistance of FCBs compared with pure Fe_2O_3 and Fe_3O_4 nanoparticles electrode. The values of the Ohmic resistance (R_Ω) and (R_{ct}) are 5.13 and 198.22 Ω for FCBs, respectively, which are lower than those of corresponding Fe_2O_3 (5.56 and 422.31 Ω) and Fe_3O_4 (9.63 and 268 Ω), respectively (Figure 6a). It may be attributed to the faster transfer rate of Li^+ ions in FCBs than that of pure Fe_2O_3 and Fe_3O_4, due to the improvement of the surface electro-conductivity of FCB nanocomposites. This phenomenon can be attributed to the excellent conductivity of C in FCBs nanocomposite. Because of the significantly enhanced conductivity of FCBs, the corresponding superior electrochemical performance in LIBs should be expected.

The electrochemical behavior of the Fe_3O_4/C microbelts was measured in the lithium-ion battery. Figure 6b shows different

cycle discharge−charge profiles for FCBs at a current rate of 0.2 C. In the first discharge curve, an extended potential plateau at about 0.8 V versus Li^+/Li is observed for the FCBs composite, accompanying the redox of Fe_3O_4 nanoparticles (Supporting Information Figure S4), similar to the literature results for Fe_3O_4.[34−40] The electrochemical reversible reaction can be summarized as the equations below.

$$FCBs + xLi^+ \leftrightarrow Li_xFCBs \tag{3}$$

$$Li_xFCBs + (8 - x)Li^+ \leftrightarrow 3Fe@C + 4Li_2O \tag{4}$$
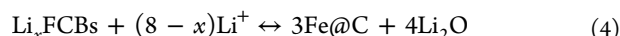
The theoretical capacity (C) of the hypothetical mixture of FCBs is calculated as follows:[54−57]

$$
\begin{aligned}
C(\text{theoretical}) &= C(Fe_3O_4) \times \text{mass percentage of } Fe_3O_4 \\
&\quad + C(\text{graphite}) \\
&\quad \times \text{mass percentage of graphite} \\
&= 924 \times 45\% + 372 \times 55\% \\
&= 622 \text{ mA h g}^{-1}
\end{aligned}
$$

The initial capacity is obtained as 1751 mA h g^{-1} for the porous FCBs, which is much higher than the theoretical capacity of Fe_3O_4 (925 mA h g^{-1}) and the theoretical prediction value for FCBs (622 mA h g^{-1}). The extra capacity in initial cycles is probably due to the decomposition of nonaqueous electrolyte during the discharge process. The large irreversible capacity observed in Figure 6b may be caused by several factors such as the conversion of Fe_3O_4 to Fe nanoparticle and the formation of amorphous Li_2O; trapped Li^+ in the inner hole of FCBs and the formation of solid electrolyte interphase (SEI) layer. The second discharge curve of the porous FCBs is different from the first, indicating significant lithium-driven structural or textural modifications similar to the reported volume expansion effect.[25] Furthermore, the charge voltage plateau of the porous FCBs is higher than the discharge. The large voltage hysteresis
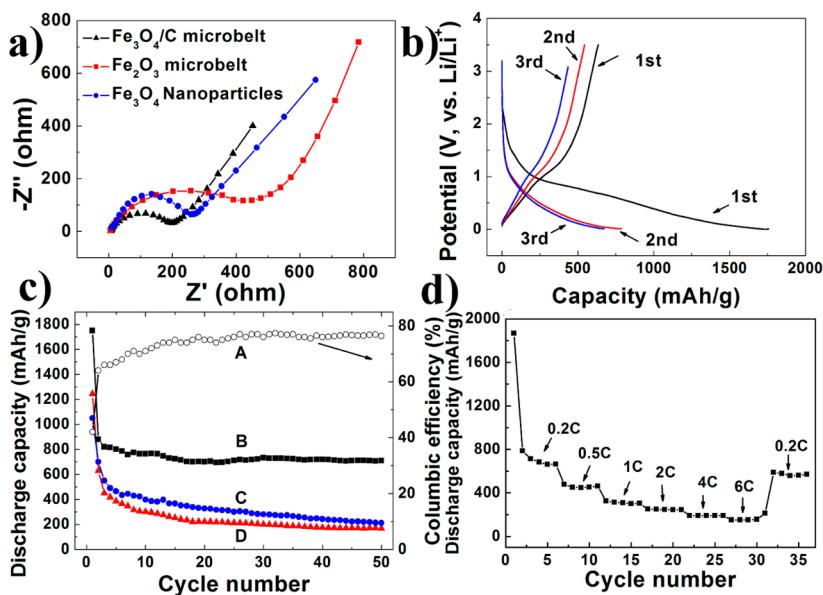

Figure 6. (a) Electrochemical impedance spectra of FCBs, α-Fe_2O_3 microbelts, and Fe_3O_4 nanoparticles electrodes before charge−discharge cycles. (b) Charge−discharge profiles of the porous FCBs at the current of 0.2 C (1 C = 500 mA g^{-1}, corresponding to the full discharge in 1 h, a rate of n C corresponds to the full discharge in $1/n$ h) in the potential range of 3.5−0.01 V at 25 °C. (c) Cyclic performance of (A and B) FCBs, (C) Fe_3O_4 nanoparticles, and (D) α-Fe_2O_3 microbelts tested at a current density of 0.2 C. (d) Charge−discharge performances of the porous FCBs at the various current rates (0.2−6 C).

polarization between charge and discharge could be due to the poor conversion reaction kinetics (i. e., limited lithium diffusion kinetics during the insertion and extraction), which is harmful to the energy efficiency of LIBs. The columbic efficiency of this cell is close to 80%, which is not high (Figure 6c). Therefore, the polarization of FCBs needs to be reduced and the columbic efficiency should be improved in future work by improving the conversion reaction kinetics, such as reducing the particle size of Fe_3O_4 and improving the porosity and conductivity of FCBs.

The second and third discharge processes exhibit reversible discharging behavior, with a little decrease of discharge capacity. The discharge capacities of the electrode in second, third, and fourth cycles are 880, 820, and 815 mA h g^{-1}, respectively (Figure 6c). The reversible capacity after 20 cycles keeps high stability and 710 mA h g^{-1} capacity is still observed up to 50 cycles (Figure 6c), which is 87% of the discharge capacity in the fourth cycle. The high reversible capacities (710 mA h g^{-1}) more than the theoretical prediction value (622 mA h g^{-1}) might be possible because the mass percentage of Fe_3O_4 provided by TG analysis is not very accurate. At higher current density (current rates of 0.5−6 C), somewhat lower discharge capacity are obtained for FCBs (Figure 6d). The discharge capacities decrease to 184 mA h g^{-1} at 6 C. After charge−discharge at high current rate (6 C), the high capacities (580 mA h g^{-1}) of the FCBs can be maintained at normal current rate (0.2 C). This result indicates that the FCBs material exhibits the excellent rate capability. For contrast, several control experiments were carried out with pure α-Fe_2O_3 microbelts with low BET surface area (21 m^2 g^{-1}, Supporting Information Figure S5) and Fe_3O_4 nanoparticles (Supporting Information Figure S6) as anode materials in LIBs at a rate of 0.2 C, which provided lower discharge capacity and recycling performance than those of the FCBs (Figure 6c).

The excellent performance of FCBs with high charge−discharge capacity and good cyclic properties in LIBs can be attributed to the highly stable porous belt structure of FCB and to the firm carbon matrix surrounded Fe_3O_4 nanoparticles. A porous FCB favors Li^+ ion transport in LIBs, and carbon layers on Fe_3O_4 nanoparticles prevent them from aggregation and could allow residual buffer space to relieve stress arising from the large volume change during Li^+ insertion/extraction. Tangled FCBs with excellent conductivity are of benefit to electron transport.

4. CONCLUSIONS

In summary, we reported a facile method for synthesis of porous Fe_3O_4/C microbelt by simple electrospinning, combined with a calcination process for the first time. SEM and TEM images show the porous character of FCBs composite, in which Fe_3O_4 nanoparticles were embedded in a carbon matrix. The N_2 adsorption/desorption isotherm shows the porous structure and high BET surface area. The composite material exhibits good cyclic performance, and the high capacity of 710 mA h g^{-1} is still maintained after 50 cycles. The charge−discharge performance at different current rate also reveals high rechargeable stability of FCBs. The excellent electrochemical performance attributes to the stability of composite structure and high electroconductivity of FCBs. The carbon matrix is of benefit to accommodate the large volume change of Fe_3O_4 nanoparticles during Li^+ insertion/extraction. The tight contact between carbon layer and Fe_3O_4 nanoparticles and the tangled FCBs improve the conductivity of the FCBs. These futures of the FCBs are the desirable characters for potential electrode

materials. The synthesis method reported here can combine several processes including porous structure, carbon wrapping, and formation of Fe_3O_4 nanoparticles in one step, which is simple and effective, and could be extended to fabricate other metal oxide and inorganic compound carbon composites.

■ ASSOCIATED CONTENT

Ⓢ Supporting Information

STEM, TEM image, and cyclic voltammetry of FCBs and SEM image, XRD pattern, and BET results of the α-Fe_2O_3 microbelt. This material is available free of charge via the Internet at http://pubs.acs.org.

■ AUTHOR INFORMATION

Corresponding Author

*E-mail: zhengxu@nju.edu.cn.

Notes

The authors declare no competing financial interest.

■ ACKNOWLEDGMENTS

■ REFERENCES

(1) Armand, M.; Tarascon, J. M. *Nature* **2008**, *451*, 652.
(2) Hwang, T. H.; Lee, Y. M.; Hong, B.-S.; Sep, J.-S.; Choi, J. W. *Nano Lett.* **2012**, *12*, 802.
(3) Wang, H.; Yang, Y.; Liang, Y.; Cui, L.; Casalongue, H. S.; Li, Y.; Hong, G.; Cui, Y.; Dai, H. *Angew. Chem., Int. Ed.* **2011**, *50*, 7364.
(4) Zhang, H.; Yu, X.; Braun, P. V. *Nat. Nanotech.* **2011**, *6*, 277.
(5) Nam, K. T.; Kim, D.; Yoo, P. J.; Chiang, C.; Meethong, N.; Hammond, P. T.; Chiang, Y.; Belcher, A. M. *Science* **2006**, *312*, 885.
(6) Poizot, P.; Laruelle, S.; Grugeon, S.; Dupont, L.; Tarascon, J.-M. *Nature* **2000**, *407*, 496.
(7) Li, Y.; Tan, B.; Wu, Y. *Nano Lett.* **2008**, *8*, 256.
(8) Lou, X. W.; Deng, D. J.; Lee, Y.; Feng, J.; Archer, L. A. *Adv. Mater.* **2008**, *20*, 258.
(9) Xiong, S.; Chen, J. S.; Lou, X. W.; Zeng, H. C. *Adv. Funct. Mater.* **2012**, *22*, 861.
(10) Meduri, P.; Pendyala, C.; Kumar, V.; Sumanasekera, G. U.; Sunkara, M. K. *Nano Lett.* **2009**, *9*, 612.
(11) Ye, J.; Zhang, H.; Yang, R.; Li, X.; Qi, L. *Small* **2010**, *6*, 296.
(12) Deng, D.; Lee, J. Y. *Chem. Mater.* **2008**, *20*, 1841.
(13) Wang, B.; Chen, J. S.; Wu, H. B.; Wang, Z.; Lou, X. W. *J. Am. Chem. Soc.* **2011**, *133*, 17146.
(14) Zhong, J.; Cao, C.; Liu, Y.; Li, Y.; Khan, W. S. *Chem. Commun.* **2010**, *46*, 3869.
(15) Chen, J.; Xu, L.; Li, W.; Gou, X. *Adv. Mater.* **2005**, *17*, 582.
(16) Chaudhari, S.; Srinivasan, M. *J. Mater. Chem.* **2012**, *22*, 23049.
(17) Xiong, Q. Q.; Tu, J. P.; Lu, Y.; Chen, J.; Yu, Y. X.; Qiao, Y. Q.; Wang, X. L.; Gu, C. D. *J. Phys. Chem. C* **2012**, *116*, 6495.
(18) Xu, J. S.; Zhu, Y. J. *ACS Appl. Mater. Interfaces* **2012**, *4*, 4752.
(19) Xiong, Q.-Q.; Tu, J.-P.; Lu, Y.; Chen, J.; Yu, Y.-X.; Wang, X.-L.; Gu, C.-D. *J. Mater. Chem.* **2012**, *22*, 18639.
(20) Jiao, F.; Bruce, P. G. *Adv. Mater.* **2007**, *19*, 657.
(21) Zhao, J.; Tao, Z.; Liang, J.; Chen, J. *Cryst. Growth Des.* **2008**, *8*, 2799.
(22) Sayle, T. X. T.; Maphanga, R. R.; Ngoepe, P. E.; Sayle, D. C. *J. Am. Chem. Soc.* **2009**, *131*, 6161.
(23) Wang, K.; Wei, M.; Morris, M. A.; Zhou, H.; Holmes, J. D. *Adv. Mater.* **2007**, *19*, 3016.
(24) Li, J.; Wan, W.; Zhou, H.; Li, J.; Xu, D. *Chem. Commun.* **2011**, *47*, 3439.

(25) Gu, M.; Li, Y.; Li, X.; Hu, S.; Zhang, X.; Xu, W.; Thevuthasan, S.; Baer, D. R.; Zhang, J.; Liu, J.; Wang, C. *ACS Nano* **2012**, *6*, 8439.

(26) Lu, L. Q.; Wang, Y. *J. Mater. Chem.* **2011**, *21*, 17916.

(27) Liu, J.; Xia, H.; Xue, D.; Lu, L. *J. Am. Chem. Soc.* **2009**, *131*, 12086.

(28) Zhang, X.; Wang, K.; Wei, X.; Chen, J. *Chem. Mater.* **2011**, *23*, 5290.

(29) Li, Y.; Zhu, S.; Liu, Q.; Gu, J.; Guo, Z.; Chen, Z.; Feng, C.; Zhang, D.; Moon, W. *J. Mater. Chem.* **2012**, *22*, 2766.

(30) Kim, D.; Lee, D.; Kim, J.; Moon, J. *ACS Appl. Mater. Interfaces* **2012**, *4*, 5408.

(31) Wang, H.; Cui, L.; Yang, Y.; Casalongue, H. S.; Robinson, J. T.; Liang, Y.; Cui, Y.; Dai, H. *J. Am. Chem. Soc.* **2010**, *132*, 13978.

(32) Li, H.; Zhou, H. *Chem. Commun.* **2012**, *48*, 1201.

(33) Piao, Y.; Kim, H. S.; Sung, Y.; Hyeon, T. *Chem. Commun.* **2010**, *46*, 118.

(34) Li, B.; Cao, H.; Shao, J.; Qu, M. *Chem. Commun.* **2011**, *47*, 10374.

(35) Zhu, T.; Chen, J. S.; Lou, X. W. *J. Phys. Chem. C* **2011**, *115*, 9814.

(36) Yang, Z.; Shen, J.; Archer, L. A. *J. Mater. Chem.* **2011**, *21*, 11092.

(37) Kang, E.; Jung, Y. S.; Cavanagh, A. S.; Kim, G.; George, S. M.; Dillon, A. C.; Kim, J. K.; Lee, J. *Adv. Funct. Mater.* **2011**, *21*, 2430.

(38) Yoon, T.; Chae, C.; Sun, Y.; Zhao, X.; Kungc, H. H.; Lee, J. K. *J. Mater. Chem.* **2011**, *21*, 17325.

(39) Zhou, G.; Wang, D.; Li, F.; Zhang, L.; Li, N.; Wu, Z.; Wen, L.; Lu, G. Q.; Cheng, H. *Chem. Mater.* **2010**, *22*, 5306.

(40) Ban, C.; Wu, Z.; Gillaspie, D. T.; Chen, L.; Yan, Y.; Blackburn, J. L.; Dillon, A. C. *Adv. Mater.* **2010**, *22*, E145.

(41) Chen, J. S.; Zhang, Y.; Lou, X. W. *ACS Appl. Mater. Interfaces* **2011**, *3*, 3276.

(42) Zhao, X.; Xia, D.; Zheng, K. *ACS Appl. Mater. Interfaces* **2012**, *4*, 1350.

(43) Chen, D.; Ji, G.; Ma, Y.; Lee, J. Y.; Lu, J. *ACS Appl. Mater. Interfaces* **2011**, *3*, 3078.

(44) Mou, F.; Guan, J.; Shi, W.; Sun, Z.; Wang, S. *Langmuir* **2010**, *26*, 15580.

(45) Miao, Y.; Wang, R.; Chen, D.; Liu, Z.; Liu, T. *ACS Appl. Mater. Interfaces* **2012**, *4*, 5353.

(46) Chen, H.; Wang, N.; Di, J.; Zhao, Y.; Song, Y.; Jiang, L. *Langmuir* **2010**, *26*, 11291.

(47) Zhu, C.; Yu, Y.; Gu, L.; Weichert, K.; Maier, J. *Angew. Chem., Int. Ed.* **2011**, *50*, 6278.

(48) McCann, J. T.; Lim, B.; Ostermann, R.; Rycenga, M.; Marquez, M.; Xia, Y. *Nano Lett.* **2007**, *7*, 2470.

(49) McCann, J. T.; Marquez, M.; Xia, Y. *J. Am. Chem. Soc.* **2006**, *128*, 1436.

(50) Lang, L.; Wu, D.; Xu, Z. *Chem.—Eur. J.* **2012**, *18*, 10661.

(51) Remiro, P. M.; Cortazar, M. M.; Calahorra, M. E. *J. Mater. Sci.* **1999**, *34*, 2627.

(52) Guo, C. X.; Yang, H. B.; Sheng, Z. M.; Lu, Z. S.; Song, Q. L.; Li, C. M. *Angew. Chem., Int. Ed.* **2010**, *49*, 3014.

(53) Wu, Z. S.; Ren, W. C.; Wen, L.; Gao, L. B.; Zhao, J. P.; Chen, Z. P.; Zhou, G. M.; Li, F.; Cheng, H. M. *ACS Nano* **2010**, *4*, 3187.

(54) Poizot, P.; Larunelle, S.; Grugeon, S.; Tarascon, M. *J. Electrochem. Soc.* **2002**, *149*, A1212.

(55) Li, D.; M€uller, M. B.; Gilje, S.; Kaner, R. B.; Wallace, G. G. *Nat. Nanotechnol.* **2008**, *3*, 101.

(56) Li, B.; Cao, H.; Shao, J.; Li, G.; Qu, M.; Yin, G. *Inorg. Chem.* **2011**, *50*, 1628.

(57) Li, B.; Cao, H.; Shao, J.; Qu, M.; Warner, J. H. *J. Mater. Chem.* **2011**, *21*, 5069.